Fluid Dynamics and Co-located Conferences
June 24-27, 2013, San Diego, CA
21st AIAA Computational Fluid Dynamics Conference

Discontinuous Galerkin Method for Compressible Viscous Reacting Flow

Yu Lv* and Matthias Ihme†
Department of Mechanical Engineering, Stanford University, Stanford, CA, 94305, USA

In the present study, a discontinuous Galerkin (DG) framework is developed to simulate chemically reacting flows. The algorithm combines a double-flux method to account for variable thermodynamic properties, a Strang-splitting scheme for the stiff reaction chemistry, a robust WENO-based shock limiter, and the non-linear viscous-diffusive transport is discretized using the BR2 method. The algorithm is verified and validated by considering a series of one- and two-dimensional test cases, and results are compared with self-similarity solutions and experiments to examine critical algorithmic components. These cases include low-Mach deflagration systems and supersonic inviscid and viscous problems. Multi-dimensional configurations consider the shock-flame interaction and detonation initiation process. It is shown that the reactive DG-method provides an accurate description of key-physical mechanisms that control the ignition onset in confined detonation systems.

I. Introduction

Over recent years, considerable progress has been made on the theoretical and computational development of Discontinuous Galerkin (DG) methods for hyperbolic conservation laws.[1,2,3,4,5] Compared to low-order finite difference/finite-volume schemes, DG-methods offer several advantages. Specifically, the DG-method (i) allows for arbitrarily high order of accuracy that is determined through the selection of the basis functions; (ii) is able to capture discontinuities and strong gradients of the solution without spurious oscillations; (iii) enables a compact discretization that is, unlike conventional FD and FV methods, confined to the local element; (iv) is well suited for advanced refinement strategies utilizing both local mesh-adaptation and refinement in polynomial order (*hp*-refinement); and (v) exhibits optimal convergence properties.

Despite these advantages, main issues towards the successful utilization of DG-method are improved robustness-requirements and the treatment of shocks and contact discontinuities.[6] Two main strategies have been proposed for shock capturing in the DG framework, namely artificial viscosity[7] and limiters. Since, however, we are interested in unsteady flow problems, the additional stiffness that is accompanied with the artificial viscosity ansatz increases the computational complexity. Therefore, the utilization of limiters appears to be a more suitable approach for application to time-dependent chemical reacting systems.

Early efforts on developing limiters for DG-methods were presented by Cockburn & Shu.[1,2] These schemes were restricted to quadratic polynomials, and over recent years, more robust limiting procedures have been reported. In particular, Zhang & Shu[8] developed a positivity-preserving limiter for DG, which has been utilized in Euler flows with source terms. Later, Wang et al.[9]

*Research Assistant, AIAA Member
†Assistant Professor, AIAA Member

simplified this method, and employed this limiter in simulations of detonation waves with one-step chemistry. Zhong & Shu[10] developed a WENO-based limiter for structured meshes. Only recently, the same group extended this limiter to unstructured tetrahedral meshes.[11]

The objective of this work is the development of a DG framework for compressible multi-component chemically reacting flows under consideration of detailed reaction chemistry and complex thermo-viscous-diffusive transport properties. This work extends previous developments for chemical reacting Euler flows.[12] The present work focuses on the fully reacting Navier-Stokes equations with particular emphasis on the viscous-diffusion discretization. Based on the above-mentioned limiting procedures, an element-local shock-capturing scheme is employed. Special attention is hereby directed towards the utilization of detailed chemical kinetics and non-linear transport properties. To this end, a Strang-splitting scheme is employed combining a time-explicit scheme for advective fluxes and a point-wise implicit scheme for advancing the stiff reactive and diffusive terms. The computational method enables the description of combustion-physical processes in the full Mach-regime, including deflagration and detonation systems.

The remainder of this paper is outlined as follows. The governing equations are presented in Sec. II, and the spatial discretization is discussed in Sec. III. Algorithmic developments regarding the treatment of non-uniform transport properties, time-integration, and shock-capturing are discussed in Sec. IV. The resulting DG-method is applied to a series of test-configurations of increasing physical complexity to demonstrate the accuracy and capability of this algorithm. The paper finishes with conclusions and a discussion of further research directions.

II. Governing Equations

The present study is concerned with the two-dimensional multi-component reacting Navier-Stokes equations. Written in vector form, these equations can be written as:

$$\partial_t \boldsymbol{U} + \partial_k \boldsymbol{F}_k^c = \partial_k \boldsymbol{F}_k^v + \boldsymbol{S}, \tag{1}$$

where $\boldsymbol{U}$ is the state-vector, $\boldsymbol{F}_k^c$ and $\boldsymbol{F}_k^v$ are the convective and viscous fluxes in the kth direction, and the source term is denoted by $\boldsymbol{S}$. These terms take the following form:

$$\boldsymbol{U} = \begin{pmatrix} \rho Y_1 \\ \vdots \\ \rho Y_N \\ \rho u \\ \rho v \\ \rho E \end{pmatrix}, \quad \boldsymbol{F}_1^c = \begin{pmatrix} \rho u Y_1 \\ \vdots \\ \rho u Y_N \\ \rho u^2 + p \\ \rho uv \\ u(\rho E + p) \end{pmatrix}, \quad \boldsymbol{F}_2^c = \begin{pmatrix} \rho v Y_1 \\ \vdots \\ \rho v Y_N \\ \rho uv \\ \rho v^2 + p \\ v(\rho E + p) \end{pmatrix}, \tag{2}$$

$$\boldsymbol{F}_1^v = \begin{pmatrix} -J_{x,1} \\ \vdots \\ -J_{x,N} \\ \tau_{xx} \\ \tau_{xy} \\ u\tau_{xx} + v\tau_{xy} - q_x \end{pmatrix}, \quad \boldsymbol{F}_2^v = \begin{pmatrix} -J_{y,1} \\ \vdots \\ -J_{y,N} \\ \tau_{yx} \\ \tau_{yy} \\ u\tau_{yx} + v\tau_{yy} - q_y \end{pmatrix}, \quad \boldsymbol{S} = \begin{pmatrix} \dot{\omega}_1 \\ \vdots \\ \dot{\omega}_N \\ 0 \\ 0 \\ 0 \end{pmatrix}, \tag{3}$$

where u, v, Y_i, E and p refer, respectively, to the velocity components in x- and y-directions, mass fraction of species i, specific total energy, and pressure. The total number of species is denoted by

N. The density ρ is evaluated as

$$\rho = \sum_{i=1}^{N} (\rho Y_i) \ , \tag{4}$$

and Eqs. (1) are complemented by a state equation, relating pressure to density, temperature, and species composition. In the present case, we consider the ideal gas law,

$$p = \rho \frac{R_u}{\overline{W}} T \ , \qquad \text{with} \qquad \overline{W} = \left(\sum_{i=1}^{N} \frac{Y_i}{W_i} \right)^{-1} \ , \tag{5}$$

where R_u is the universal gas constant, W_i is the molecular weight of species i, and $\overline{W}$ is the mean molecular weight. The specific total energy of the mixture is given by:

$$E = \sum_{i=1}^{N} Y_i \left(h^0_{f,i} + \int_{T_0}^{T} c_{p,i}(T) dT \right) + \frac{1}{2} \left(u^2 + v^2 \right) - \frac{p}{\rho}, \tag{6}$$

where $h^0_{f,i}$ and $c_{p,i}$ denote the heat of formation and specific heat capacity of the ith species, respectively. The specific heat capacity is temperature-dependent and evaluated in terms of a polynomial expression.[13]

The viscous-diffusive terms, appearing in Eqs. (1), are written as:

$$J_{k,i} = -\rho D_i \partial_k Y_i \ , \tag{7a}$$

$$\tau_{kl} = \mu(\partial_k u_l + \partial_l u_k) - \frac{2}{3} \mu \delta_{kl} \partial_m u_m \ , \tag{7b}$$

$$q_k = -\kappa \partial_k T \ , \tag{7c}$$

in which the diffusive flux $J_{k,i}$ is represented using Fick's law, the viscous stress tensor is represented by Newton's law, and the conductive heat-flux is modeled using Fourier's law. In Eqs. (7), D_i refers to the mixture-averaged diffusivity of the ith species, μ is the dynamic viscosity, and κ is the mixture conductivity. These transport properties are evaluated using Chemkin transport libraries.[14]

III. Discontinuous Galerkin Discretization

To develop a discontinuous Galerkin, we start by writing the reactive Navier-Stokes equations in index form:

$$\partial_t U_j + \partial_k F^c_{kj} - \partial_k F^v_{kj} - S_j = 0, \tag{8}$$

where U_j refers to the jth component of the conservative state vector, and F^c_{kj} and F^v_{kj} are the corresponding jth component of the inviscid and viscous flux along the kth spatial dimension. F^c_{kj} is a non-linear function of the full state vector, and F^v_{kj} can be linearized with respect to the gradients of the conservative variables.

A spatial discretization is then obtained by partitioning the computational domain Ω into a set of non-overlapping cells $\{\Omega_e\}$ with boundaries $\partial\Omega_e$. Then, we consider the finite-dimensional functional space $\mathcal{V}^p_h$, with

$$\mathcal{V}^p_h = \{\phi | \phi \in H^1(\Omega_e), \phi \in \mathcal{P}^p(\Omega_e) \ \forall \Omega_e \in \mathcal{T}_h\} \ , \tag{9}$$

where $\mathcal{T}_h$ is the mesh partition, and $\mathcal{P}^p$ denotes the space of polynomial functions of degree p. The solution to U_j is approximated by the polynomial space as:

$$U^h_j(t, \boldsymbol{x}) = \sum_{q=1}^{N_p} \widetilde{U}_{j,q}(t) \phi_q(\boldsymbol{x}) \ , \tag{10}$$

where $\widetilde{U}_{j,q}(t)$ is the time-dependent coefficient of the qth expansion term. A variational formulation is then obtained by multiplying Eq. (8) by a test function ϕ and integrated over each element,

$$\left(\int_{\Omega_e} \phi_r \phi_q de\right) \partial_t \widetilde{U}_{j,q}(t) + \int_{\Omega_e} \phi_r \partial_k F^c_{kj} de - \int_{\Omega_e} \phi_r \partial_k F^v_{kj} de - \int_{\Omega_e} \phi_r S_j de = 0 \,. \tag{11}$$

In this equation, the first term on the left-hand-side (LHS) is the mass matrix and the fourth term is element-local and can be directly evaluated using quadrature rule.

The second term is the advection term, and is treated by partial integration:

$$\int_{\Omega_e} \phi_r \partial_k F^c_{kj} de = -\int_{\Omega_e} \partial_k \phi_r F^c_{kj} de + \int_{\partial\Omega_e} \phi^+_r \widehat{F}^c_{kj}(U^+_j, U^-_j)\widehat{n}_k ds \,, \tag{12}$$

where $\widehat{n}_k$ is the outward pointing normal on $\partial\Omega_e$. On $\partial\Omega_e$, the notation $()^+$ and $()^-$ refers to the quantities taken from the interior and exterior of element Ω_e, respectively. The elements are essentially tied to each other through the numerical flux $\widehat{F}^c_{kj}$, which is here discretized using an HLLC flux.[15]

The viscous-diffusive flux, appearing as the third term on the LHS of Eq. (11), includes second-order derivatives. This term is linearized and expressed in terms of the conserved state-variables:

$$F^v_{kj} = A_{klji} \partial_l U_i \tag{13}$$

with index i and l referring to the state-vector and spatial dimension, respectively. The fourth-order tensor A_{klji} accounts for the differentiation of the viscous flux with respect to $\partial_l U_i$. The discretization of the viscous term follows the second form of Bassi & Rebay (BR2),[16] which takes the following form:

$$-\int_{\Omega_e} \phi_r \partial_k F^v_{kj} de = \int_{\Omega_e} \partial_k \phi_r F^v_{kj} de - \int_{\partial\Omega_e} \phi^+_r \widehat{F}^v_{kj} \widehat{n}_k ds \,, \tag{14}$$

and the first term can be further expand as,

$$\begin{aligned} \int_{\Omega_e} \partial_k \phi_r F^v_{kj} de &= -\int_{\Omega_e} \partial_l\big(\partial_k \phi_r A_{klji}\big) U_i de + \int_{\partial\Omega_e} \partial_k \phi^+_r A^+_{klji} \hat{U}_i \hat{n}_l ds & (15a) \\ &= \int_{\Omega_e} \partial_k \phi_r A_{klji} \partial_l U_i de - \int_{\partial\Omega_e} \partial_k \phi^+_r A^+_{klji}\big(U^+_i - \hat{U}_i\big)\hat{n}_l ds \,. & (15b) \end{aligned}$$

The two terms on the right-hand-side (RHS) of Eq. (15*b*) represent the interior contribution and the dual consistency term, and the second term on the RHS of Eq. (14) refers to the viscous flux across two neighboring elements. The notation $\widehat{\cdot}$ refers to the flux function at each discontinuity between two elements. The selection of these flux functions is not arbitrary. By considering the stability properties, the following flux function is used in BR2:

$$\widehat{F}^v_{kj} = \{A_{klji}\partial_l U_i\} - \eta\{\delta_{kj}\} \qquad \text{and} \qquad \widehat{U}^h_i = \{U^h_i\} \tag{16}$$

where the operator $\{\cdot\} := \frac{1}{2}\big((\cdot)^+ + (\cdot)^-\big)$ is the mean value across the element face, η is a constant and δ_{kj} is a stabilization term that is associated with the element faces. In the BR2-method, δ_{kj} is determined by solving the following local problem on each edge:

$$\int_{\Omega^+_e} \delta^+_{kj} \phi_r de + \int_{\Omega^-_e} \delta^-_{kj} \phi_r dx = \int_{\partial\Omega_e} \big(\phi_r A_{klji}\big)\big(U^+_i - U^-_i\big)\hat{n}_l ds \tag{17}$$

where $\partial\Omega_e$ denotes the face associated with the elements Ω^+_e and Ω^-_e. With this treatment, the discretization yield a compact stencil with good stability properties.

IV. Algorithmic Developments

A. Treatment of Variable Thermodynamic Properties

The dependence of thermodynamic properties on temperature for a set of selected species is shown in Fig. 1(a). Since the specific heat capacity has a direct effect on the combustion temperature and species conversion, the commonly employed calorically perfect gas approximation cannot be used. Therefore, variable and temperature-dependent thermodynamic properties require consideration.

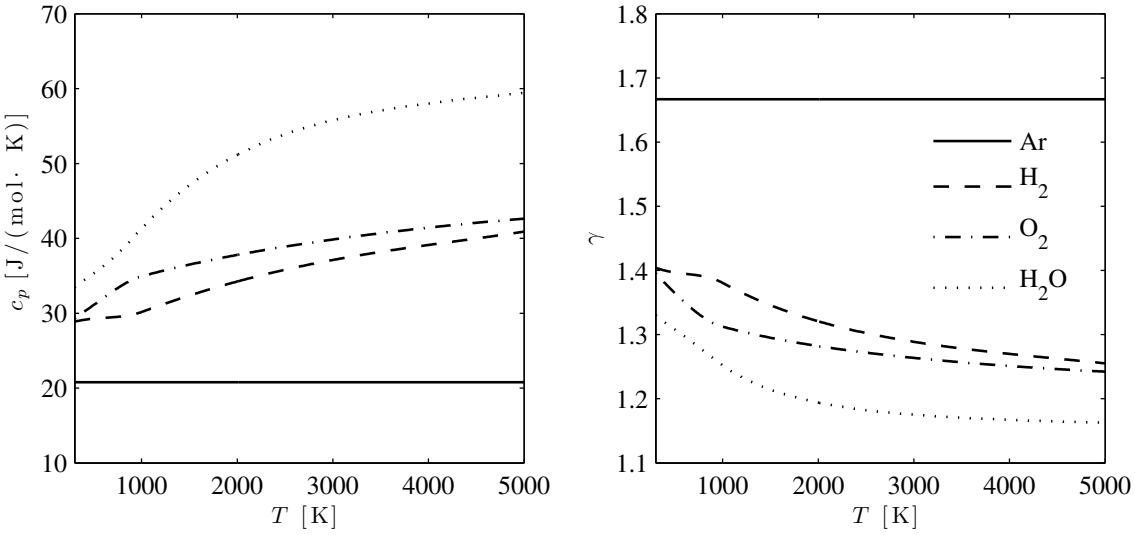

(a) Specific heat capacity.

(b) Adiabatic index.

Figure 1. Illustration of temperature-dependence of thermodynamic properties, showing (a) constant-pressure mole-specific heat capacity and (b) adiabatic index.

However, it has been recognized that the consideration of variable thermodynamic properties introduces spurious oscillations in fully-conservative flux formulations.[17,18,19,20,21,22] This issue appears to be more severe in the DG-method due to the higher-order discretization and associated lower dispersion and dissipation properties. To address this issue, we will use the double-flux model that was originally developed by Billet & Ryan.[23] The key-idea of the double-flux method is the construction of an intermediate state in which all thermal properties are frozen during the time-step increment $[t, t + \Delta t]$. To completely avoid spurious oscillations, piecewise profiles of the ratio of specific heat capacities, γ, are assumed in each element. Furthermore, this treatment only affects convective hyperbolic operators and does not influence diffusion and source terms. Utilizing this model requires the reformulation of the specific total energy in the form that resembles the perfect gas model.

By writing $c_p^k = a^k T + b^k$ for $T \in [T^k, T^{k+1}]$, we can express the enthalpy as:

$$h = h_f^0 + \sum_{k=0}^{m-1} \int_{T^k}^{T^{k+1}} (a^k T + b^k) dT + \int_{T_m}^{T} (a^m T + b^m) dT \,, \tag{18}$$

and by precomputing the specific enthalpy over the discretized subintervals spanning $T_0 \leq T \leq T^m$ we can write the above equation as:

$$h = \widehat{h_0^m} + c_p(T) T \,, \tag{19}$$

where $\widehat{h_0^m}$ combines the heat of formation and the integrated sensible enthalpy h_s^m. With this, we can write the specific total energy for the mixture in a form that is equivalent to that of a calorically perfect gas:

$$E = \widehat{h_0} + \frac{p}{\rho(\gamma - 1)} + \frac{u_j^2}{2} \, .$$

With this, the procedure for evaluating the flux over the time-interval $[t, t + \Delta t]$ is summarized as follows:

1. Compute and store γ and $\rho\widehat{h_0}$ on each element
2. Compute the interior convection term in Eq. (12) using γ, and the boundary flux for two adjacent elements as:

$$F_j^+ = F(U_j^+, U_j^-, \gamma^+, \rho\widehat{h}_0^+) \, , \tag{20a}$$

$$F_j^- = F(U_j^+, U_j^-, \gamma^-, \rho\widehat{h}_0^-) \tag{20b}$$

3. Repeat step 2 for every sub-stage of the specified time marching scheme
4. Update γ and $\rho\widehat{h_0}$ at the new time step $t + \Delta t$
5. With least-square, correct the energy polynomial representation using updated values for γ and $\rho\widehat{h_0}$.

B. Treatment of Stiff Reaction Chemistry

The development of computationally efficient numerical schemes for combustion requires the consideration of chemical species that evolve on vastly different time-scales. Therefore, a splitting scheme is used in which the non-stiff convection and diffusion operators are advanced using an explicit scheme and the stiff chemical source terms are treated implicitly. The splitting scheme can formally be written as:

$$\boldsymbol{U}(t + \Delta t) = e^{0.5\Delta t F_k^c} e^{0.5\Delta t F_k^v} e^{\Delta t S} e^{0.5\Delta t F_k^v} e^{0.5\Delta t F_k^c} \boldsymbol{U}(t) \tag{21}$$

where the solution operator $e^{tF}u_0$ denotes $d_t u = F(u)$ with initial condition $u(0) = u_0$. In this scheme, the time step is solely controlled by the convection operator based on the CFL criterion. The CFL number for different polynomial representations follows $1/(2p + 1)$. An implicit ODE solver is employed for evaluating the reaction operator $e^{\Delta t S}$, and a strong stability-preserving Runge-Kutta method[1] is used for evaluating the convection and diffusion operators, $e^{\Delta t F_k^c}$ and $e^{\Delta t F_k^v}$, respectively.

C. Shock-Capturing Scheme

To represent discontinuities, the weighted essentially non-oscillatory (WENO) based limiter for quadrilateral elements by Zhong & Shu[24] is used, exhibiting good accuracy-preserving properties in smooth regions and robust shock-capturing capabilities. The limiter proceeds in two step: In the first step, so-called troubled cells are identified using a shock-detector. In the second step, the polynomial solution in the troubled cells are limited using information from its corresponding neighbor cells. This is done in characteristic space by diagonalizing the local flux Jacobian matrix $\mathbf{A}_j = \frac{\partial \mathbf{F}^c}{\partial \boldsymbol{U}}|_{\bar{U}_j}$. By denoting the left and right eigenvectors as $\mathbf{R}^{-1}$ and $\mathbf{R}$, the local characteristic variables are evaluated as $\boldsymbol{V} = \mathbf{R}^{-1}\boldsymbol{U}$. After limiting $\boldsymbol{V}$ in polynomial space using the WENO-procedure,[24] this state-vector is transformed back into physical coordinates. To apply this

procedure to flows with variable thermodynamic properties, additional compatibility conditions require consideration and these have been reported in Lv & Ihme.[12] Furthermore, it has been pointed out that the limiter acting on characteristic variables cannot guarantee the positivity of the pressure value when transformed back into physical space. Therefore, to enhance the robustness of the algorithm, the positivity preserving limiter[25] is adopted on troubled elements after the above limiting has been conducted.

V. Numerical Test Cases

In the following sections, a series of one- and two-dimensional test cases are consider in order to examine the performance and accuracy of the developed reactive DG-formulation. We start by considering three chemical inert compressible flow-field configuration in Sec. A, which is followed by presenting simulation results for three reacting configurations. Throughout this investigation, quantitative comparisons with experimental data or reported simulation results are presented.

A. Non-Reactive Test Cases

1. *Shu-Osher Problem*

The performance of the limiter is tested with a modified Shu-Osher problem. This problem considers the interaction of a $M = 3$ shock with an entropy wave. Written in non-dimensional form, the one-dimensional computational domain is $x \in [-5, 5]$ and initial conditions are:

$$(\rho, u, p, Y_{\mathrm{He}}, Y_{\mathrm{N_2}})^T = \begin{cases} (3.8571, 2.6294, 10.3333, 0, 1)^T & \text{if } x \leq -4, \\ (1 + 0.2\sin(5x), 0, 1, 1, 0)^T & \text{if } x > -4. \end{cases} \tag{22}$$

The computational domain is discretized using 200 elements, and Fig. 2 shown simulation results for linear and quadratic polynomials at the non-dimensional time $t = 1.8$. In this figure, open symbols are simulation results, and the solid line refers to the "exact" solution, which is obtained from a DG-solution with $p = 2$ and a discretization having 200 elements. This comparison shows that significant improvements in accuracy can be obtained with increasing polynomial order. Further, the benefit of the high-order polynomial representation is not deteriorated by the limiting procedure.

2. *Two-dimensional Shock Diffraction at 90°-Corner*

The limiter and high-order polynomial representation are further tested in a 2D shock diffraction case. In this case, a shock with a Mach number of 2.4 is expanded over a 90° corner.[26] The detailed problem configuration and related experimental results are presented in Fig. 3. In this case, two different element sizes, namely $\Delta x/D = 0.01$ and $\Delta x/D = 0.005$, are used for convergence analysis, and linear and quadratic polynomials are considered. Computational results on the fine mesh are shown in Fig. 4 for both polynomial solution orders. Compared to measurements,[26] the simulation results correctly reproduce the wave interaction around the corner. Even for this problem with corner-singularity, the limiting procedure remains robust. The benefit of the high-order scheme is apparent, which is most notable in the region of the vortex recirculation (see Figs. 4 and 5(a)). The computed value of minimum density in the corner vortex is used for validation. Comparisons with results by Hillier[27] and Riplet et al.[28] are presented in Fig. 5(b), showing good agreement and convergence to the reference data for increasing polynomial order.

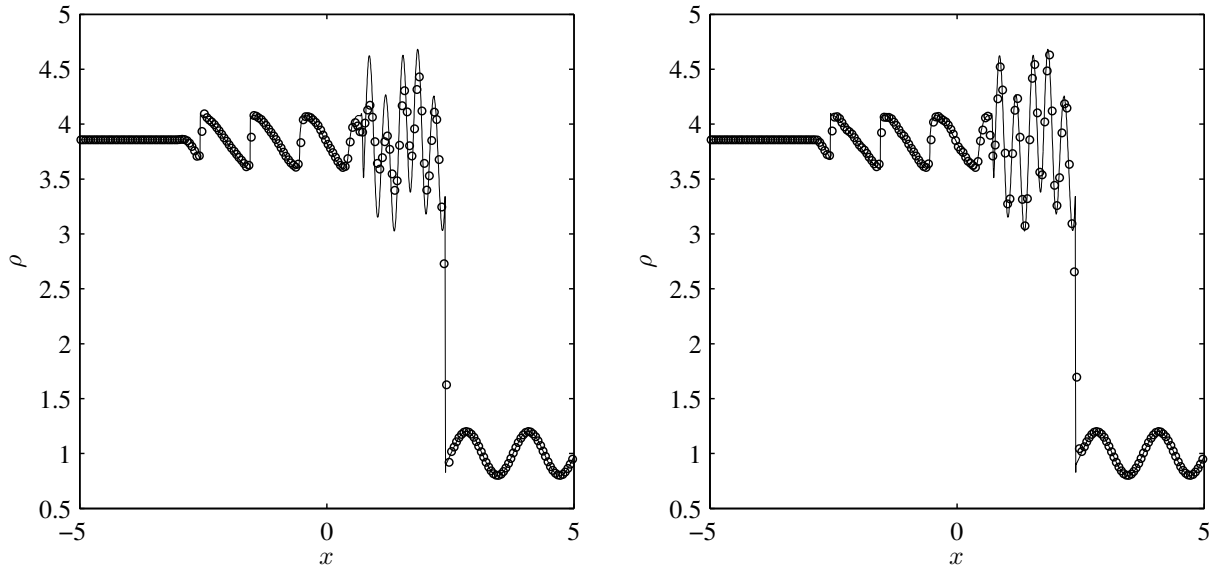

(a) $p = 1$ (b) $p = 2$

Figure 2. Simulation results for the multi-component shock/density-wave interaction problem at $t = 1.8$, showing density profiles for (a) linear polynomial ($p = 1$) and (b) quadratic polynomial ($p = 2$) basis functions. Open symbols are simulation results, and the solid line refers to the "exact" solution.

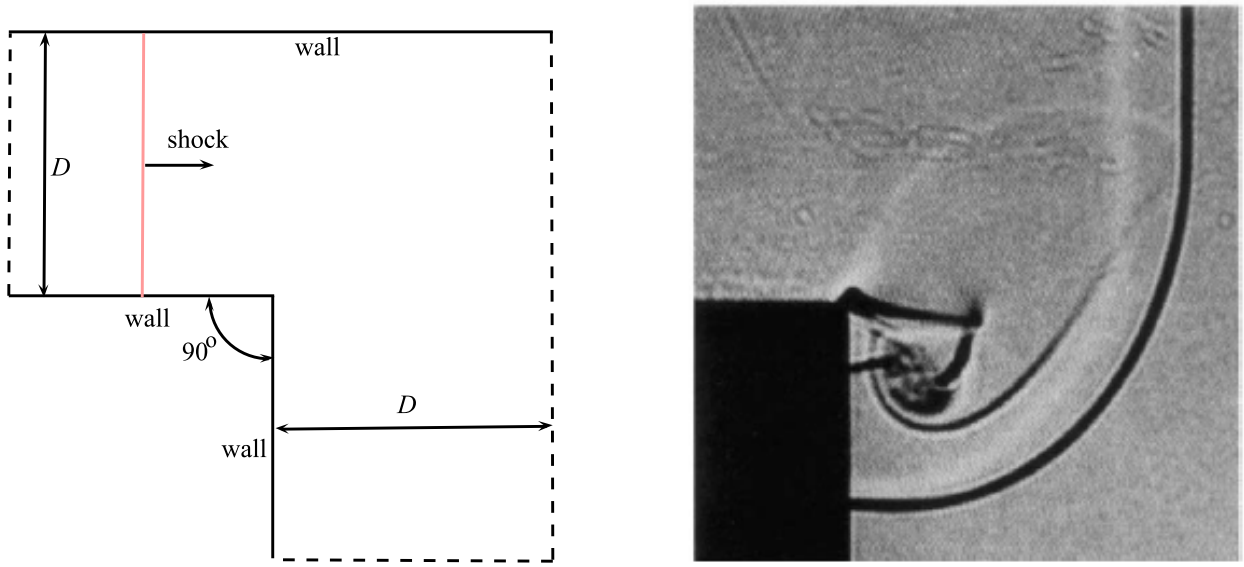

(a) Schematic of shock diffraction problem. (b) Schlieren measurements.

Figure 3. Schematic of configuration and experimental results[26] for a shock-diffraction problem with initial shock Mach number of 2.4.

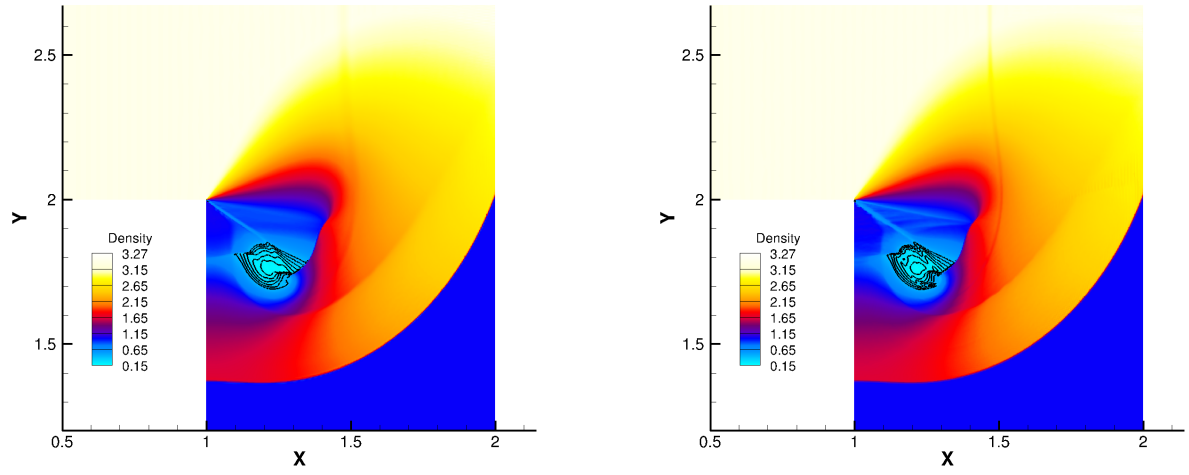

(a) Polynomial order: $p = 1$.

(b) Polynomial order: $p = 2$.

Figure 4. Instantaneous density fields for shock-diffraction case using (a) linear and (b) quadratic polynomial order; contour lines are evenly distributed.

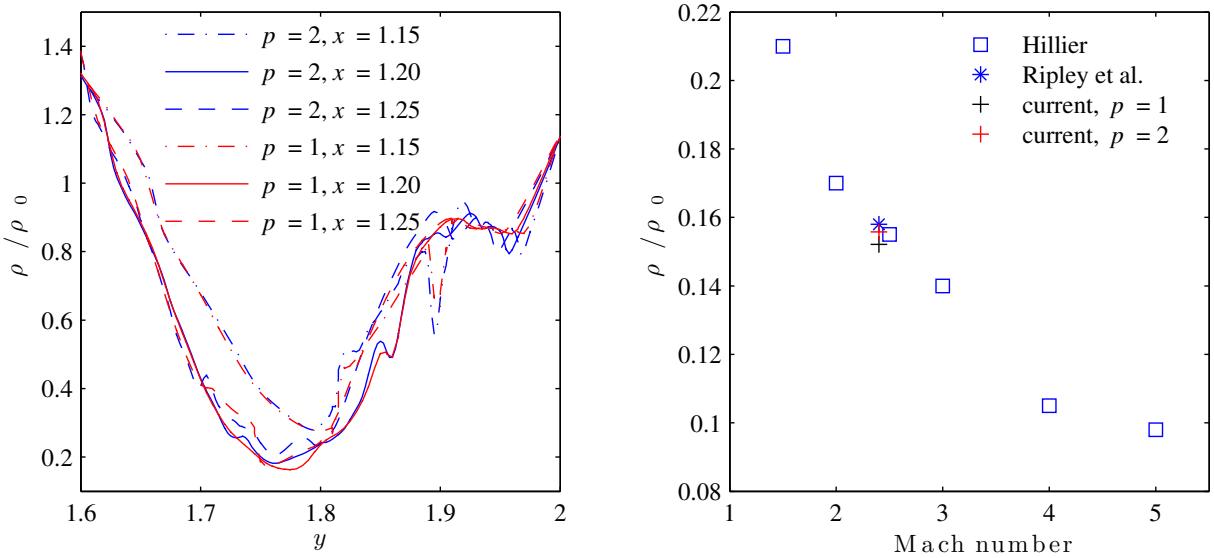

(a) Density profile across diffraction region.

(b) Minimum density inside corner vortex.

Figure 5. (a) Density profiles for the shock diffraction case and (b) comparisons of minimum density location with reference data by Hillier[27] and Ripley et al.[28]

3. *Supersonic Laminar Boundary Layer*

This two-dimensional test case examines the implementation of the viscous fluxes in conjunction with the limiting procedure. To this end, we consider a supersonic free stream boundary layer at a Mach number of 2.0. In this configuration, an adiabatic wall boundary condition is imposed at the bottom, and all other sides are treated by Neumann boundaries. Simulations with linear and quadratic polynomial order are performed. Parameters that are used for the simulation are summarized in Tab. 1. The viscosity is computed using Sutherland's law and the Prandtl number is set to a value of 0.75. The global Reynolds-number evaluated with respect to the length of the domain is $\mathrm{Re}_L = 100$ and the element size is $\Delta x/\delta_L = \Delta y/\delta_L = 0.16$, where δ_L is the boundary layer thickness at the end of the computation domain which is computed as $\delta_L = 1.978L/\sqrt{\mathrm{Re}_L}$ according to the self-similarity assumption.[29]

Simulation results are presented in Figs. 6-7. The instantaneous temperature field is presented in Fig. 7, showing the formation of a shockwave that is anchored at the inlet of the domain. Comparisons of temperature profiles in wall-normal direction for different polynomial discretizations and the solution of self-similarity are presented in Fig. 7. From this comparison it can be seen that the results for $p = 1$ and $p = 2$ are both in good agreement with the similarity solution. A quantitative analysis showed that the higher-order discretization provides a more accurate description of the temperature in the near-wall region.

u_e [m/s]	T_e [K]	p_e [Pa]	Ma_e	ν_e [m^2/s]
639	289	123616	1.875	1.204×10^{-5}

Table 1. Simulation parameters and operating conditions for the compressible laminar boundary layer simulation.

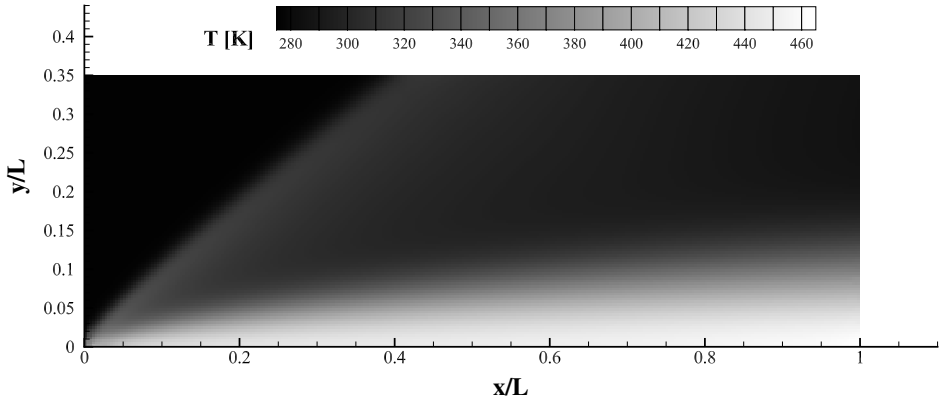

Figure 6. Computed temperature field for compressible laminar adiabatic boundary layer.

B. Reactive Test Cases

1. *One-dimensional Hydrogen/Oxygen/Argon Deflagration System*

The objective of this configuration is to evaluate the viscous implementation using nonlinear transport properties, the assessment of the hyperbolic operator at low-Mach number conditions, and algorithmic compatibility with the detailed chemistry solver. To this end, a one-dimensional $H_2/O_2/Ar$

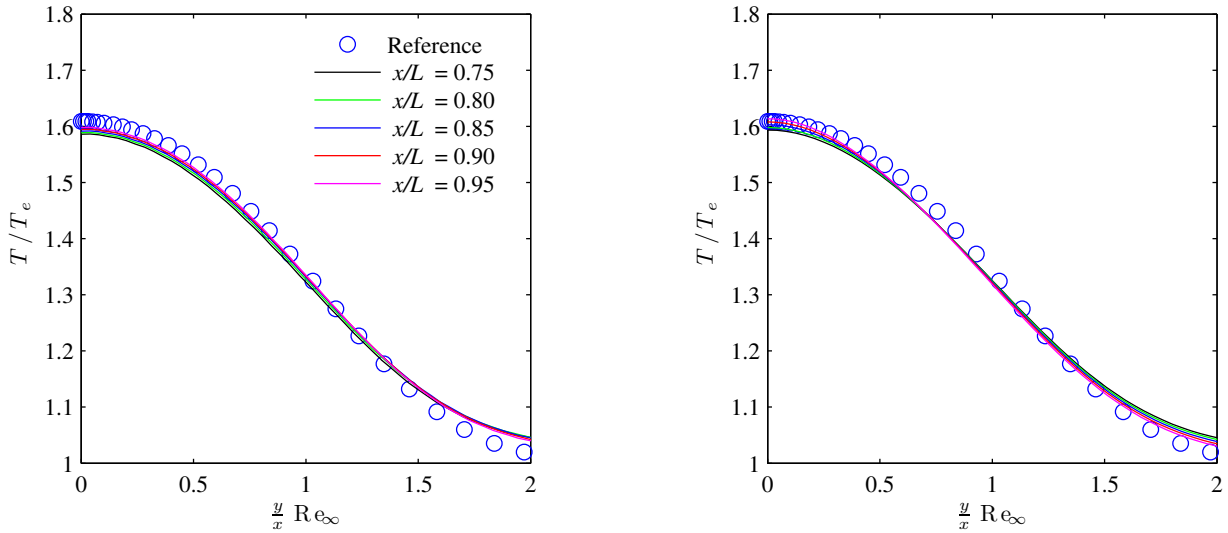

(a) Polynomial order: $p = 1$.

(b) Polynomial order: $p = 2$.

Figure 7. Comparison of wall-normal temperature profiles for (a) linear and (b) quadratic polynomial order. Symbols denotes self-similar solution based on the approaches in book.[29]

deflagration system at a molar ratio of 2:1:7 is considered. The conditions in the unburned mixture are $p = 1$ bar and $T = 300$ K. The reaction chemistry is described by the detailed chemical mechanism due to Westbrook,[30] consisting of 9 species and 34 elementary reaction steps. To avoid acoustic reflections at the boundaries, a characteristic-based non-reflective boundary condition is imposed at the left side. The temperature field is initialized using a tangent hyperbolic profile. As shown in Fig. 8, the flame gradually reaches a constant propagation speed after ignition.

Comparisons of the computed flame speed for different spatial resolutions and polynomial orders are summarized in Tab. 2. The prediction is further verified by comparing against CHEMKIN results as shown in Fig. 9. In all computations the flame-speed is evaluated at the location at which the temperature is equal to 400 K. The predicted flame speed from CHEMKIN is 1.111 m/s.

	$\Delta x = 100\mu$m	$\Delta x = 50\mu$m
$p = 1$	0.1897 m/s	1.210 m/s
$p = 2$	1.205 m/s	1.204 m/s

Table 2. Comparison of the computed flame speed obtained for different mesh-resolutions and polynomial orders.

2. One-dimensional Viscous Detonation System

This test-case combines all algorithmic developments to simulate a viscous detonation system under consideration of detailed reaction chemistry. For this case, we consider the same $H_2/O_2/Ar$ mixture as in the previous study, but initial pressure and temperature are now set to 6670 Pa and 298 K. The spatial discretization is identical to that used in the previous section. The mixture is initialized by the Chapman-Jouguet jump condition, and after a transitional period the mixture ignites, resulting in the formation of a stationary Zeldovich-von Neumann-Döring (ZND) detonation structure.

The detonation speed is evaluated by tracking the detonation front-location, which is here associated with the temperature of 400 K. Figure 10 shows temperature profiles of the converged

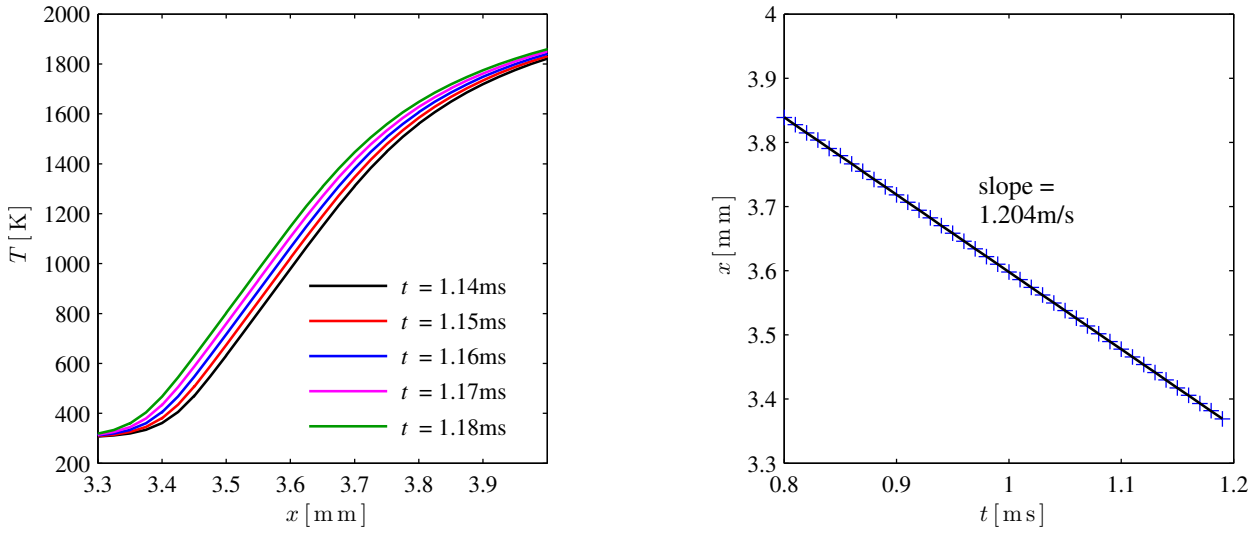

(a) Temperature profiles

(b) Space-time diagram of flame location.

Figure 8. Temperature and space-time diagram for one-dimensional $H_2/O_2/Ar$ deflagration system ($p = 2$, $\Delta x = 50\mu$m).

solution obtained on a mesh with element size of 50 μm and quadratic polynomial representation.

From Fig. 10(b) it can also be seen that the detonation front propagates at a constant speed. Since this problem does not have any analytic solution, a convergence study is first conducted using different grid sizes and polynomial order. The converged solution is then compared to the inviscid calculation that was reported by Lv & Ihme.[12] The computed detonation speed are summarized in Tab. 3. Figure 11 provides a more detailed comparison of the detonation structure, showing temperature, density, and species mass fraction of hydroxyl and molecular hydrogen. At the shock front, the improvement in the shock resolution by increasing the spatial resolution can be observed. The representation of the reaction zone using quadratic polynomial basis functions results in comparable accuracy as linear polynomials on the finer grid.

	$\Delta x = 100\mu$m	$\Delta x = 50\mu$m
$p = 1$	1633.3 m/s	1655.2 m/s
$p = 2$	1649.5 m/s	1654.3 m/s

Table 3. Comparison of detonation speed for different grid resolutions and polynomial orders; Argon-diluted H_2/O_2 mixture.

3. Two-dimensional Shock/Flame Interaction

The objective of this test case is to demonstrate the capability of the developed DG framework for application to multi-dimensional flow-field simulations. For this, we consider a shock-flame interaction configuration that was also consider by Taylor et al.[31] The setup is shown in Fig. 12. The geometry mimics a shock tube configuration with a length of 22.8 mm in stream wise direction, and 7.6 mm in height. Symmetric boundary conditions are applied at the center plane so that only the upper half of the domain is considered in the simulation. The domain is initially filled with a stoichiometric hydrogen/air mixture at 1 atm and 300 K. To facilitate ignition, a cylindrical kernel

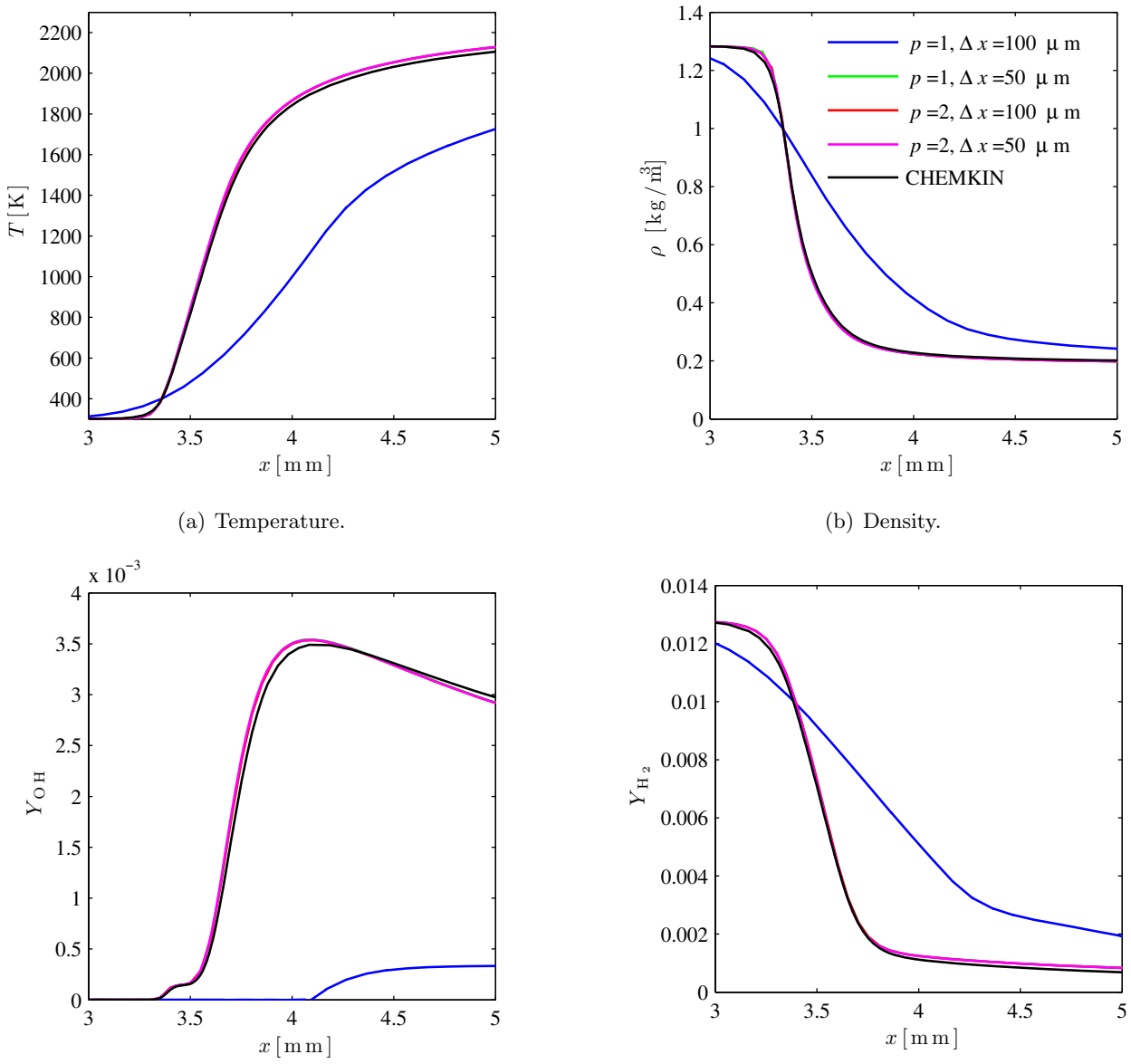

(a) Temperature.

(b) Density.

(c) OH mass fraction.

(d) H_2 mass fraction

Figure 9. Comparison of deflagration flame structure for different polynomial representations and spatial resolutions, and CHEMKIN reference solution.

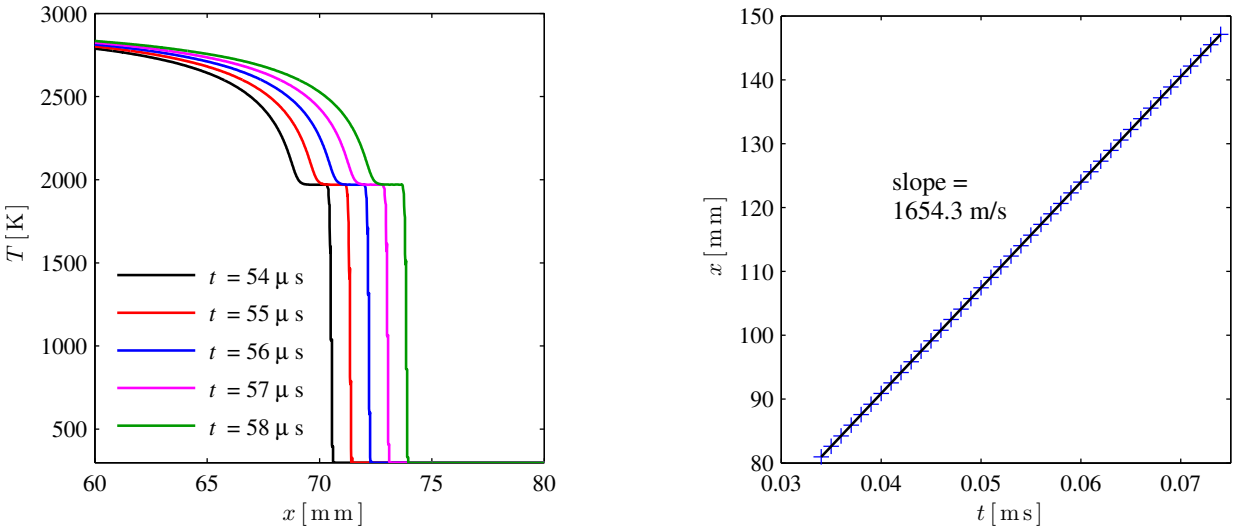

(a) Temperature profile.

(b) Flame location.

Figure 10. $H_2/O_2/Ar$ mixture detonation flame evolution along simulation time ($p = 2$, $\Delta x = 50\mu$m)

of equilibrium reaction products is placed inside the domain. The kernel has a radius of 3 mm and is located 11.7 mm away from the end-wall. A shock wave with a Mach number of 2.8 is initially imposed at 7.7 mm from the left boundary. The shock wave propagates to the right, where it interacts with the cylindrical flame kernel and is eventually reflected at the end-wall. To simulate this configuration, we consider quadratic polynomial basis functions ($p = 2$) and the element size is $\Delta x = \Delta y = 25\mu$m (corresponding to 138,624 elements). The reaction chemistry is described by the recently updated high-pressure hydrogen-mechanism due to Burke et al.[32] Simulations with and without consideration of viscous effects are performed for comparisons. All walls are treated as no-slip conditions for the viscous simulations while slip-walls are prescribed for the inviscid simulation.

Simulation results are presented in Fig. 13, showing on the left to viscous results, and results of the Euler simulation are given on the right. The simulations capture all critical features that are associated with the viscous heating and flame initialization process. Compared with the inviscid computation, the viscous simulations show that the ignition is initiated by the viscous heating in the boundary layer, resulting in the formation of a deflagrative ignition kernel away from the end-wall. Furthermore, shock bifurcation is observed in the viscous case which is a result of the interaction of the reflected shock/detonation wave with the boundary layer. The ignition in the inviscid case is followed by a detonation wave, while the viscous case follows a transition process from deflagration to a detonation mode. These mechanisms that are predicted with the DG-method are qualitatively consistent with denotation physics. However, additional simulations and refinement studies are necessary to further assess convergence, and this is the subject of future research.

VI. Conclusion

In this contribution, a discontinuous Galerkin method is developed for the simulation of compressible viscous multi-component flows with detailed reaction chemistry. The algorithm combines a double-flux method to account for variable thermodynamic properties, a Strang-splitting scheme for the stiff reaction chemistry, a robust WENO-based shock limiter, and the non-linear viscous-

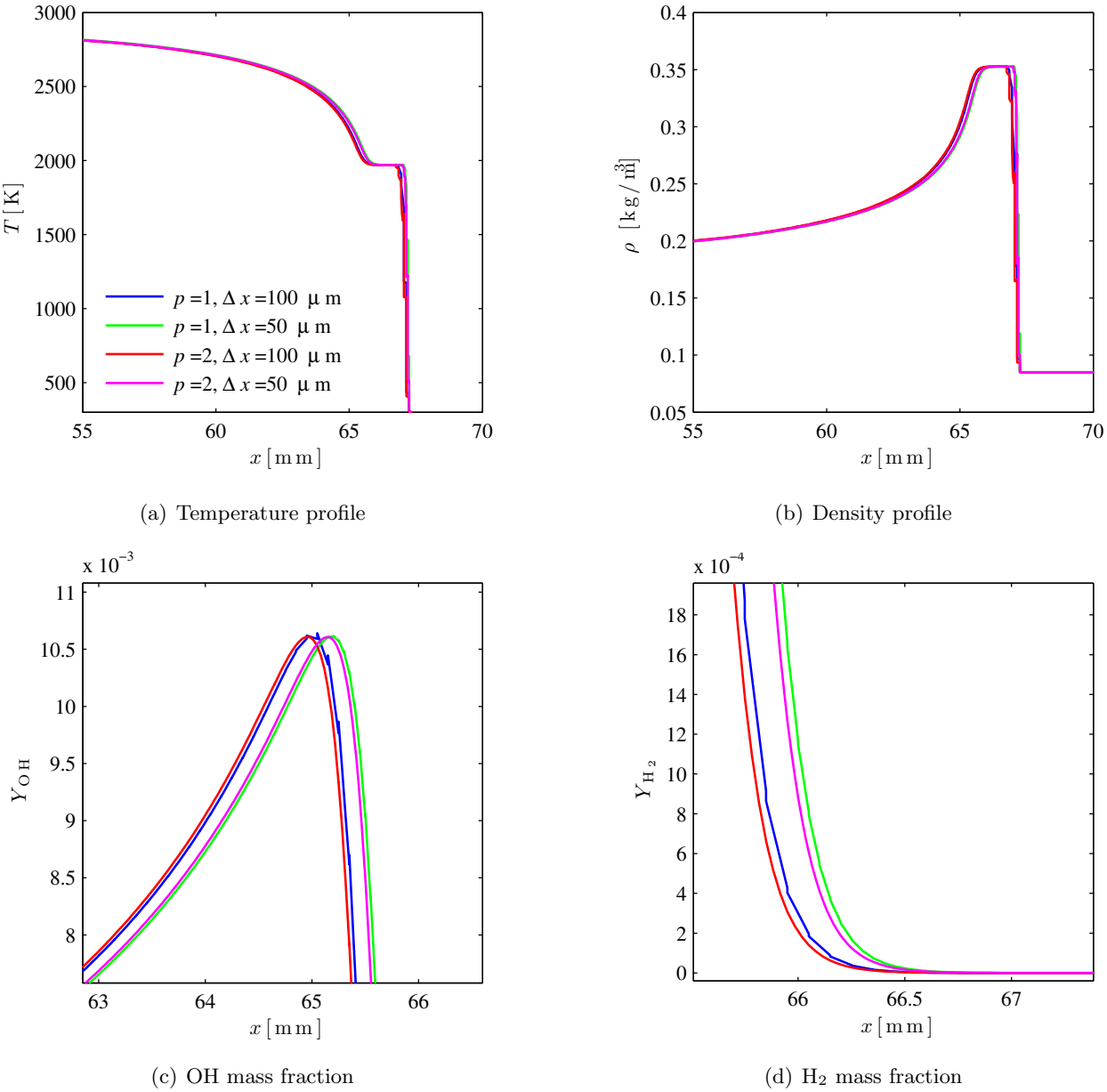

(a) Temperature profile

(b) Density profile

(c) OH mass fraction

(d) H_2 mass fraction

Figure 11. Comparison of the current prediction to CHEMKIN calculation

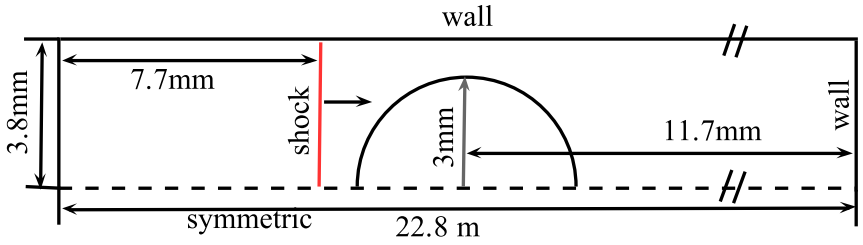

Figure 12. Simulation setup for two-dimensional shock flame interaction case

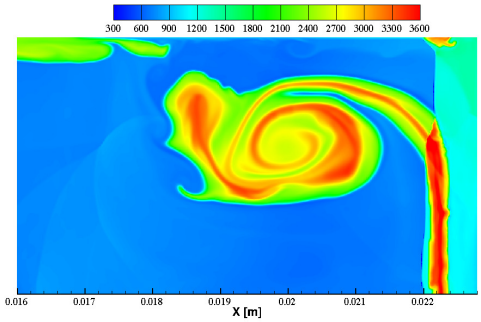

(a) Navier-Stokes, $t = 14\mu$s

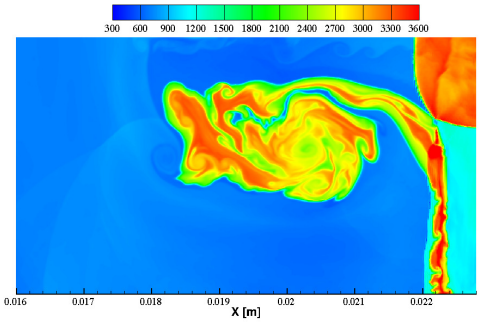

(b) Euler, $t = 14\mu$s

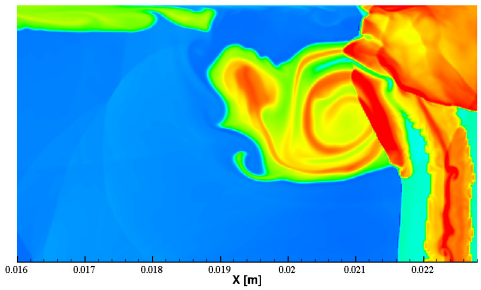

(c) Navier-Stokes, $t = 15\mu$s

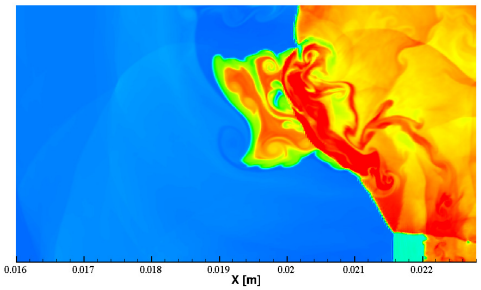

(d) Euler, $t = 15.2\mu$s

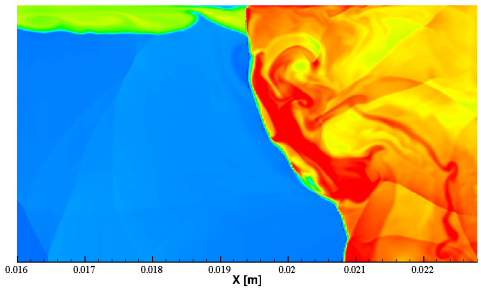

(e) Navier-Stokes, $t = 16\mu$s

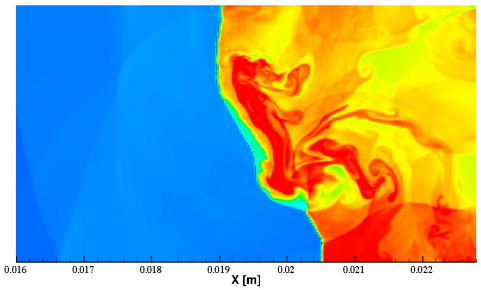

(f) Euler, $t = 16\mu$s

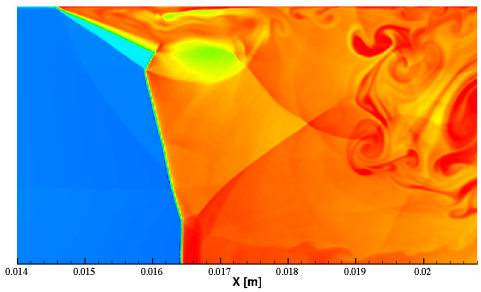

(g) Navier-Stokes, $t = 19\mu$s

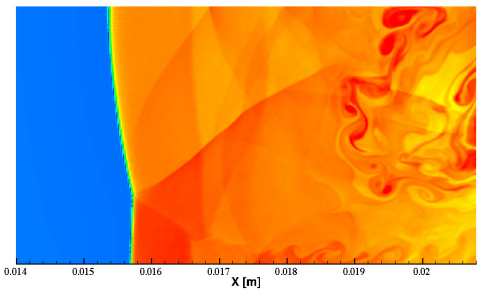

(h) Euler, $t = 19.2\mu$s

Figure 13. Comparison of the viscous and inviscid cases

diffusive transport is discretized using the BR2 method. A series of one- and two-dimensional test cases are considered to assess the performance and accuracy of this DG-algorithm. These cases included low-Mach deflagration systems and supersonic inviscid and viscous problems. The multi-dimensional configurations considered the shock-flame interaction and detonation initiation process. It was shown that the reactive DG-method provides an accurate description of key-physical mechanisms that control the ignition onset in confined detonation systems.

Acknowledgments

Financial support through the NSF CAREER program with Award No. CBET-0844587 is gratefully acknowledged.

References

[1]Cockburn, B. and Shu, C. W., "TVB Runge-Kutta local projection discontinuous Galerkin finite element method for conservation laws III: One dimensional systems," *Journal of Computational Physics*, Vol. 84, 1989, pp. 90–113.

[2]Cockburn, B. and Shu, C.-W., "TVB Runge-Kutta local projection discontinuous Galerkin finite element method for conservation laws II: General framework," *Journal of Scientific Computing*, Vol. 52, No. 186, 1989, pp. 411–435.

[3]Cockburn, B. and Shu, C.-W., "Runge-Kutta discontinuous Galerkin methods for convection-dominated problems," *Journal of Scientific Computing*, Vol. 16, No. 3, 2001, pp. 173–261.

[4]Cockburn, B., Karniadakis, G. E., and Shu, C.-W., "The development of discontinuous Galerkin methods," *Discontinuous Galerkin Methods*, edited by B. Cockburn, G. E. Karniadakis, and C.-W. Shu, Springer, 1999, pp. 3–50.

[5]Cockburn, B., "Discontinuous Galerkin methods for computational fluid dynamics," *Encyclopedia of Computational Mechanics*, edited by R. Borst, E. Stein, and T. Hughes, Vol. 3, John Wiley & Sons, Ltd., England, 2004, pp. 91–123.

[6]Shu, C.-W., "High-order finite difference and finite volume WENO schemes and discontinuous Galerkin methods for CFD," *International Journal of Computational Fluid Dynamics*, Vol. 17, No. 2, 2003, pp. 107–118.

[7]Persson, P. and Peraire, J., "Sub-cell shock capturing for discontinuous Galerkin methods," AIAA paper 2006-1121, 2006.

[8]Zhang, X. and Shu, C.-W., "Positivity-preserving high order discontinuous Galerkin schemes for compressible Euler equations with source terms," *J. Comp. Phys.*, Vol. 230, No. 4, 2011, pp. 1238–1248.

[9]Wang, C., Zhang, X., Shu, C.-W., and Ning, J., "Robust high order discontinuous Galerkin schemes for two-dimensional gaseous detonations," *J. Comp. Phys.*, Vol. 231, No. 2, 2012, pp. 653–665.

[10]Zhong, X. and Shu, C.-W., "A simple weighted essentially nonoscillatory limiter for Runge-Kutta discontinuous Galerkin methods," *Journal of Computational Physics*, Vol. 232, No. 1, 2013, pp. 397–415.

[11]Zhu, J., X., Z., Shu, C., and Qiu, J., "Runge-Kutta discontinuous Galerkin method using a new type of WENO limiters on unstructured meshes," *Journal of Computational Physics*, Vol. 248, No. 1, 2013, pp. 200–220.

[12]Lv, Y. and Ihme, M., "Development of discontinuous Galerkin method for detonation and supersonic combustion," AIAA paper 2013-0688, 2013.

[13]McBride, B. J., Zehe, M. J., and Gordon, S., "NASA Glenn Coefficients for Calculating Thermodynamic Properties of Individual Species," NASA/TP-2002-211556, NASA Glenn Research Center, Cleveland, Ohio, 2002.

[14]Kee, R. J., Rupley, F. M., Miller, J. A., Coltrin, M. E., Grcar, J. F., Meeks, E., Moffat, H. K., Lutz, A. E., Dixon-Lewis, G., Smooke, M. D., Warnatz, J., Evans, G. H., Larson, R. S., Mitchell, R. E., Petzold, L. R., Reynolds, W. C., Caracotsios, M., Stewart, W. E., and Glarborg, P., "Chemkin Collection, Release 3.5," 1999.

[15]Toro, E., Spruce, M., and Speares, W., "Restoration of the contact surface in the HLL-Riemann solver," *SW*, Vol. 4, No. 1, 1994, pp. 25–34.

[16]Bassi, F. and Rebay, S., "GMRES discontinuous Galerkin solution of the compressible Navier-Stokes equations," *Discontinuous Galerkin Methods: Theory, Computation and Applications*, edited by K. Cockburn and Shu, Springer, Berlin, 2000, pp. 197–208.

[17]Shyue, K. M., "An efficient shock-capturing algorithm for compressible multicomponent problems," *J. Comp. Phys.*, Vol. 142, 1998, pp. 208–242.

[18]Wang, S. P., Anderson, M. H., Oakley, J. G., Corradini, M. L., and Bonazza, R., "A thermodynamically consistent and fully conservative treatment of contact discontinuities for compressible multicomponent flows," *J. Comp. Phys.*, Vol. 195, 2004, pp. 528–559.

[19]Fedkiw R., Aslam T., M. B. and Osher, S., "A non-oscillatory Eulerian approach to interface in multi material flows (the ghost fluid method)," *J. Comp. Phys.*, Vol. 152, 1999, pp. 457–492.

[20]Mulder, W. Osher, S. and Sethian, J., "Computing interface motion: The compressible Rayleigh-Taylor and Kelvin-Helmholtz instabilities," *J. Comp. Phys.*, Vol. 100, 1992, pp. 209–228.

[21]Abgrall, R., "How to prevent pressure oscillations in multicomponent flow calculations: A quasi conservative approach," *J. Comp. Phys.*, Vol. 125, 1996, pp. 150–160.

[22]Johnsen, E. and Ham, F., "Preventing numerical errors generated by interface-capturing schemes in compressible multi-material flow," *J. Comp. Phys.*, Vol. 231, No. 17, 2012, pp. 5705–5717.

[23]Billet, G. and Ryan, J., "A Runge-Kutta discontinuous Galerkin approach to solve reactive flows: The hyperbolic operator," *J. Comp. Phys.*, Vol. 230, No. 4, 2011, pp. 1064–1083.

[24]Zhong, X. and Shu, C.-W., "A simple weighted essentially nonoscillatory limiter for Runge-Kutta discontinuous Galerkin methods," *J. Comp. Phys.*, Vol. 232, 2013, pp. 397–415.

[25]Wang, C., Zhang, X., Shu, C.-W., and Ning, J., "Robust high order discontinuous Galerkin schemes for two-dimensional gaseous detonations," *J. Comp. Phys.*, Vol. 231, No. 2, 2012, pp. 653–665.

[26]Oertel Sr., H. and Oertel Jr., H., "Optische Strömungsmeßtechnik," Karlsruhe: Braun Verlag, 1988.

[27]Hillier, R., "Computation of shock wave diffraction at a ninety degrees convex edge," *Shock Waves*, Vol. 1, 1991, pp. 89–98.

[28]Ripley, R. C., Lienb, F.-S., and Yovanovich, M. M., "Numerical simulation of shock diffraction on unstructured meshes," *Computers & Fluids*, Vol. 35, No. 10, 2006, pp. 1420–1431.

[29]White, F. M., *Viscous Fluid Flow*, McGraw-Hill, Inc, 1991.

[30]Westbrook, C. K., "Chemical kinetics of hydrocarbon oxidation in gaseous detonations," *Combust. Flame*, Vol. 46, 1982, pp. 191–210.

[31]Taylor, B. D., Houim, R. W., Kessler, D. A., Gamezo, V. N., and Oran, E. S., "Detonation Initiation and Shock-Flame Interaction in Hydrogen-Air Mixtures," AIAA Paper 2013-1171, 2013.

[32]Burke, M., Chaos, M., Ju, Y., Dryer, F., and Klippenstein, S., "Comprehensive H2/O2 Kinetic Model for High-Pressure Combustion," *International Journal of Chemical Kinetics*, Vol. 44, 2012, pp. 444–474.